Computational Model of Magnesium Deposition and Dissolution for Property Determination via Cyclic Voltammetry

Alexander F. Chadwick,[a,b,*] Gulin Vardar,[a,b] Stephen DeWitt,[b,c,*] Alice E. S. Sleightholme,[d] Charles W. Monroe,[b,e,] Donald J. Siegel,[a,b,c,f,**] and Katsuyo Thornton[a,b,c,**,z]**

[a]*Department of Materials Science and Engineering, University of Michigan, Ann Arbor, Michigan 48109, USA*
[b]*Joint Center for Energy Storage Research, USA*
[c]*Applied Physics Program, University of Michigan, Ann Arbor, Michigan 48109, USA*
[d]*Department of Chemical Engineering, University of Michigan, Ann Arbor, Michigan 48109, USA*
[e]*Department of Engineering Science, University of Oxford, Oxford OX1 3PJ, United Kingdom*
[f]*Department of Mechanical Engineering, University of Michigan, Ann Arbor, Michigan 48109, USA*

The development of a practical magnesium-anode battery requires electrolytes that allow for highly efficient magnesium exchange while also being compatible with cathode materials. Here, a one-dimensional continuum-scale model is developed to simulate cyclic plating/stripping voltammetry of a model magnesium-based electrolyte system employing magnesium borohydride/dimethoxyethane [$Mg(BH_4)_2$/DME] solutions on a gold substrate. The model is developed from non-electroneutral dilute-solution theory, using Nernst-Planck equations for the mass flux and Poisson's equation for the electrostatic potential. The electrochemical reaction is modeled with multistep Butler-Volmer kinetics, with a modified current/overpotential relationship that separately accounts for the portions of the current responsible for nucleating new deposits and propagating or dissolving existing ones. The diffusivities of the electrolyte species, standard heterogeneous rate constant, charge-transfer coefficient, formal potential, and nucleation overpotential are determined computationally by reproducing experimental voltammograms. The model is computationally inexpensive and therefore allows for broad parametric studies of electrolyte behavior that would otherwise be impractical.

Manuscript submitted April 22, 2016; revised manuscript received June 10, 2016. Published June 23, 2016. This was Paper 341 presented at the Chicago, Illinois, Meeting of the Society, May 24–28, 2015.

A rechargeable magnesium battery was first demonstrated 25 years ago when Gregory et al.[1] showed that magnesium could be reversibly deposited onto and dissolved from a magnesium-metal surface, as well as intercalated into and deintercalated from various host cathodes. Further interest in secondary magnesium batteries arose following the work of Aurbach et al.,[2] which demonstrated a highly efficient organohaloaluminate electrolyte using a magnesium anode and a Mo_6S_8 Chevrel-phase cathode. As a battery anode, magnesium metal offers important advantages over both intercalation compounds and lithium metal, including a higher theoretical volumetric energy capacity (3833 mAh/cm^3 vs. 2046 mAh/cm^3 for lithium metal and 760 mAh/cm^3 for graphite-based lithium-ion anodes), as well as a higher abundance in the earth's crust.[3] Additionally, magnesium is less prone to dendrite formation than lithium when electrodeposited and therefore offers potential for improved battery cycle life and safety.[4]

In addition to high-capacity electrode materials, a practical magnesium battery will also require an efficient electrolyte that is compatible with (i.e., chemically stable in contact with) these electrodes. Compared to lithium electrolytes, magnesium electrolytes remain in a relatively early developmental stage.[1–29] Electrolytes formulated from Grignard reagents have been widely studied both in the battery and general electrochemistry communities.[1,6,28,30–35] The speciation of these electrolytes is complex because, in addition to ionic dissociation, the reagents also undergo the Schlenk equilibrium process (a type of ligand exchange) and form multimeric species in many solvents. Both organohaloaluminates and the so-called magnesium aluminum chloride complex (MACC) are electrolyte classes that relate closely to Grignard reagents; both include a Lewis acid, such as $AlCl_3$, to facilitate dissociation and shift the Schlenk equilibrium. Organohaloaluminates are typically of the form $RMgX + AlCl_3$, and MACC is typically of the form $MgCl_2 + AlCl_3$.[2,7,8,11,12,27] Due to their halide content, Grignards, organohaloaluminates, and MACC are corrosive to non-noble metal substrates, which presents a challenge to their practical application in batteries.[14] To avoid this problem, inorganic salts such as $Mg(TFSI)_2$ and $Mg(BH_4)_2$ in solutions based on traditional solvents[10,15–17,19–21] or ionic liquids[22–24,26] have also been explored.

Despite the recent growth in efforts to develop efficient magnesium electrolytes, many challenges remain. For example, formation of ion-blocking passivation films on magnesium surfaces and compatibility with cathode materials (allowing reversible intercalation of Mg^{2+}) both remain challenges.[3,11,13,20,36] Development of accurate electrochemical models of magnesium electrolytes, including how they interact with electrodes, could provide the insight needed to guide a search for the optimal electrolyte.

The electrochemical performance of any electrolyte depends strongly on various properties. Pinpointing which parameters most strongly impact performance can be a challenge, however. To date, only limited property values are available in the literature. For example, diffusivities have been reported for an organohaloaluminate in THF[8] and for $Mg(TFSI)_2$, $Mg(BF_4)_2$, and $Mg(BH_4)_2$ in a small number of solvents.[21] Estimates of the nucleation overpotential for magnesium deposition on different metal substrates[4,37,38] have also been presented. Development of a computational model for the plating and stripping of magnesium may be helpful, both to identify currently unexplored properties and to examine how these properties influence performance.

This paper demonstrates an efficient computational approach for simultaneously determining several key electrolyte properties such as ion diffusivities, kinetic properties such as heterogeneous rate constants, charge-transfer symmetry factors, and nucleation overpotentials, and equilibrium properties such as formal reaction potentials. By providing an understanding of how these factors impact plating/stripping kinetics, the approach may be utilized to propose optimal parameter values that would lead to improved battery performance.

Several models have been proposed to simulate the kinetics of electrodeposition and electrodissolution of metals. Wheeler et al.[39] employed the level-set method in two dimensions to examine the deposition of copper and to track the location of the metal/electrolyte interface, the movement of which was governed by Butler-Volmer kinetics. Guyer et al.[40,41] reported a thermodynamically derived

*Electrochemical Society Student Member.
**Electrochemical Society Member.
[z]E-mail: kthorn@umich.edu

one-dimensional (1D) phase-field model of metal deposition that included charge-separation effects in the double layer and was able to recover the behavior described by Butler-Volmer kinetics. Additional phase-field models have also been derived in two or three dimensions to examine deposition of copper,[42] lithium,[43–45] zinc,[46] and, most recently, magnesium.[25] All of these models have increased scientific understanding of the rich set of phenomena observed during electrodeposition and electrodissolution. Nevertheless, they are commonly limited by high computational cost, which can hinder parameterization efforts as well as the rapid determination of physical properties of materials based on the model results.

This paper presents a new continuum-scale model that is computationally inexpensive which can be employed to determine parameters describing both transport dynamics in the liquid electrolyte and interfacial reactions. The model is used to simulate cyclic voltammetry (CV) of a magnesium borohydride/dimethoxyethane ($Mg(BH_4)_2$/DME) electrolyte on a gold substrate. In the following sections, we formulate the model's governing equations, outline the numerical methods by which these equations are solved, and describe the batch data-processing procedure employed to fit simulated CV curves to experimental data. The experimental methodology employed to obtain CV data is then described. Finally, the experimental and simulation results are provided, along with a discussion of the general utility of the model. This work demonstrates the model's applicability in parameterizing the electrolyte properties.

Theory

One common approach to modeling electrochemical systems is to apply dilute solution theory to describe the electrolyte. Generally, this approach involves treating the solvent as a species in great excess and solving the set of equations that govern the material balances for each solute species i,

$$\frac{\partial c_i}{\partial t} = -\nabla \cdot \mathbf{J}_i \qquad [1]$$

where c_i is the concentration, $\mathbf{J}_i$ the total molar flux (a vector quantity), and t is time. Nernst-Planck equations are adopted as constitutive laws for mass transport,[47–49]

$$\mathbf{J}_i = -D_i \nabla c_i - z_i c_i \frac{D_i F}{RT} \nabla \phi \qquad [2]$$

where D_i is the diffusion coefficient, z_i is the charge, F is Faraday's constant, R is the ideal gas constant, T is the absolute temperature, and ϕ is the local electrostatic potential. We note that the Nernst-Einstein relationship[50] has also been employed to eliminate the electrochemical mobility as a degree of freedom here. The two terms on the right-hand side of Eq. 2 correspond to contributions from diffusion and migration, respectively; it is assumed that convection is negligible in the overall mass transport. Poisson's equation relates the electrostatic potential in the electrolyte to the local charge density, $\rho = F \sum z_i c_i$, as

$$\nabla^2 \phi = -\frac{\rho}{\epsilon_0 \epsilon_s} \qquad [3]$$

where ϵ_0 is the permittivity of free space and ϵ_s is the dielectric constant of the electrolyte.[50] When combined, Eqs. 1 through 3 form the Poisson-Nernst-Planck (PNP) system of equations.

Due to the nonlinearity and extreme stiffness of the PNP equations, simplifications are typically made to permit analytical solutions. Such simplifications include those by Cottrell[51,52] and Nicholson and Shain.[53] These theories typically assume an electrolyte that contains supporting species to eliminate electrostatic migration and do not allow for mass transfer to occur between the electrolyte and the electrode. Therefore, they do not apply to magnesium deposition and thus numerical models must be employed.

There have been substantial efforts to develop efficient methods for solving the time-dependent PNP equations numerically. As in the analytical models, simplifying approximations have commonly been used to improve numerical efficiency, such as electroneutrality of the electrolyte, which may be expressed as $\rho = 0$,[25,46,50,54,55] or that the current density, $\mathbf{i}$, is solenoidal, $\nabla \cdot \mathbf{i} = 0$.[25,50] Cohen and Cooley[56] presented one of the earliest attempts to solve the PNP equations numerically by assuming electroneutrality and adding a displacement current proportional to the time derivative of the electric field to the expression describing local current density. They then solved the resulting system of equations using an explicit finite difference method (FDM) with a predictor-corrector scheme. Sandifer and Buck[57] extended Cohen and Cooley's approach[56] by solving for the electrostatic potential with an implicit scheme, resulting in a mixed explicit/implicit scheme for the complete system of equations. A limitation of explicit FDMs is that there is a maximum time-step size above which numerical instability ensues. Brumleve and Buck[58] noted that the limitation to small time steps made simulations of large electrochemical systems expensive and implemented a fully implicit FDM to allow larger time steps, using Newton-Raphson iteration to solve the Nernst-Planck and displacement-current equations simultaneously. Streeter and Compton[59] employed a similar method, substituting the fully implicit stencil with a semi-implicit Crank-Nicolson stencil for the concentration evolution to study weakly supported potential-step experiments. They also solved Poisson's equation, rather than assuming electroneutrality or implementing a displacement-current equation. Dickinson et al.[60] subsequently modified the methodology of Streeter and Compton[59] to simulate CV of idealized single-electron transfer reactions at a hemispherical working electrode. Their model also assumed that the electrolyte was weakly to strongly supported and that no mass was transferred from the electrolyte to the electrode.

This work builds upon the methodology of Dickinson et al.[60] by extending the interfacial reaction model to account for the nucleation, growth, and dissolution of metal deposits, as well as the experimental Coulombic efficiency. The utility of the model is demonstrated by identifying parameter sets that are consistent with experimentally obtained CV data. With this validation, the model could be employed in the future to determine how parameters may differ between different electrolyte systems that are under consideration for metal-anode battery applications.

Model Formulation

The present methodology derives from the work of Dickinson et al.[60] with several modifications, listed below. First, the electrolyte is taken to be unsupported. Second, the overall redox reaction is taken to comprise a sequence of two single-electron transfers, each governed by Butler-Volmer kinetics. Third, mass exchange between the electrolyte and electrode surface is allowed. Fourth, the model includes descriptions of both the nucleation behavior of magnesium and its Coulombic efficiency. Finally, the cell geometry is taken to be planar; this has an advantage in that it makes the ohmic loss between the working and reference electrode more precise, but a disadvantage in that the diffusion boundary layer may extend well into the electrolyte.[50] Within the present 1D model, the counter electrode is assumed to be sufficiently far away from the reference electrode that the diffusion boundary layer extending from it does not impact the concentration field at the reference electrode during the duration of a CV sweep. In practice, experimental cells must be carefully designed so that these approximations are satisfied.

Since a planar cell was not available, experiments were performed in a standard three-compartment electrochemical cell, and the resulting data were used to parameterize the model. Fitting of data from the three-compartment cell serves to demonstrate the methodology as a proof-of-concept. These promising results will hopefully stimulate interest in performing experiments that correspond to the geometry assumed in simulations.

Model electrochemical half-cell.—The model describes an electrochemical half-cell comprising a working electrode (WE), a reference electrode (RE), and a region of electrolyte between them. A 1D model geometry is assumed, which approximates flat planar electrodes separated by a distance that is small in comparison to the size of

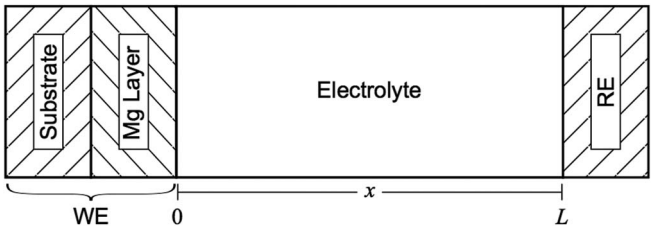

Figure 1. A schematic representation of the model domain (not to scale). Within the electrolyte, the concentrations of each electrolyte species are tracked along with the local electrostatic potential. The surface of the working electrode (WE), which is a combination of the substrate and deposited magnesium layer, is at $x = 0$, while the surface of the reference electrode (RE) is at $x = L$.

the electrode surface. This model geometry is similar to those used in many experimental cells for battery material testing, such as coin cells or Swagelok cells. However, such cells would typically not include a reference electrode and would likely have a smaller spacing between the working and counter electrodes than is assumed here.

Magnesium is deposited and dissolved from the WE, which is assumed to be an ideal noble metal that does not participate in the reaction. Initially, we assume that there is no magnesium deposited upon the surface of the WE. A schematic representation of the model system is presented in Fig. 1. The origin ($x = 0$) of the coordinate system is defined as the interface between the WE or deposited layer and the electrolyte. The surface of the reference electrode (RE) is defined to reside at position $x = L$. The counter electrode is not explicitly considered in the model; it is assumed that the counter electrode is far enough away from the WE and RE such that it does not influence the response at either electrode. In cases where this assumption is not valid, the model can be modified to account for the counter electrode.

The electrolyte is assumed to be $Mg(BH_4)_2$ in dimethoxyethane (DME), a member of the glyme series. According to Mohtadi et al.,[15] dissociation of the salt in solution is governed by the equilibrium reactions

$$Mg(BH_4)_2 \rightleftharpoons Mg(BH_4)^+ + BH_4^- \quad [4]$$

$$Mg(BH_4)^+ \rightleftharpoons Mg^{2+} + BH_4^- \quad [5]$$

where the equilibrium concentration of each species is determined by K_{d1} and K_{d2}, the respective dissociation constants of Eqs. 4 and 5. Both K_{d1} and K_{d2}, and therefore the exact species concentrations, are unknown. It is generally believed that other metal borohydride salts exist in solution as a combination of solvated ions as well as solvated ion pairs.[61,62] In addition, Mohtadi et al.[15] determined via IR and NMR spectroscopy that while further dissociation occurs in DME than in THF, it is still unlikely that complete dissociation of $Mg(BH_4)_2$ occurs in solution. Here, it is assumed that the salt is mostly dissociated to its constituent ions, but if the actual speciation differs, the approach may require corresponding modifications. It is assumed that the redox couple for the electrodeposition and electrodissolution reaction is composed of two sequential single-electron transfers involving the Mg^{2+} ion produced by Eq. 5,

$$Mg^{2+} + e^- \rightarrow Mg_i^+ \quad [6]$$

$$Mg_i^+ + e^- \rightarrow Mg \quad [7]$$

where Mg_i^+ is an unstable intermediate. The overall half-reaction is

$$Mg^{2+} + 2e^- \rightarrow Mg \quad [8]$$

where metallic magnesium is deposited upon the WE.

Electrolyte species concentration and electrostatic potential.— The model physics are described by the 1D Cartesian forms of Eqs. 1 through 3. To fully specify the solution of the boundary value problem, it is necessary to define boundary conditions on these equations. At the boundary between the WE and the electrolyte (at $x = 0$), it is assumed that the eventual thickness of the deposited magnesium layer is significantly smaller than the WE/RE separation, and thus it is assumed to be stationary in time. No reactions occur at the boundary between the electrolyte and RE (at $x = L$). The system size, L, is sufficiently large such that the combined diffusion/migration front does not reach the RE at the end of the simulation time. Therefore, rather than assuming a no-flux boundary condition, the concentration of each species can be set to its nominal bulk concentration for simplicity,

$$c_i|_{x=L} = c_{i,\text{bulk}} \quad [9]$$

The boundary condition at the WE surface ($x = 0$) is dependent upon whether or not a given species is involved in the electron transfer reaction. For inert species, a no-flux boundary condition is imposed:

$$J_i|_{x=0} = 0 \quad [10]$$

while for Mg^{2+}, the current is proportional to the current density, i:

$$J_{Mg^{2+}}\big|_{x=0} = i/2F \quad [11]$$

The zero-field approximation[59,63] is taken to govern the electrostatic potential at the WE surface,

$$\left.\frac{\partial \phi}{\partial x}\right|_{x=0} = 0 \quad [12]$$

which assumes that the thickness of the double layer is negligible in comparison to the extent of the diffusion layer in the electrolyte, and thus the potential drop across the double layer does not substantially contribute to the potential difference between the WE and zero-field plane. For sufficiently large time and length scales, Streeter and Compton[59] concluded that the zero-field approximation was in agreement with a previously described dynamic double layer model.[64] The potential is set to a constant at the RE surface ($x = L$), and we choose the value to be zero for convenience:

$$\phi|_{x=L} = 0 \quad [13]$$

If there is significant variation of the electrolyte concentration at this boundary, assuming a fixed potential may introduce some amount of error in the calculated formal reaction potential. This error is on the order of 10 mV, which is small compared to the uncertainties introduced by the differences between the model geometry and the experimental geometry.

Reaction kinetics.— The current density is taken to relate to total (surface and concentration) overpotential through a reaction rate law. To account for the multistep reaction, Butler-Volmer equations are written for both reaction steps in Eqs. 6 and 7 in the form employed by Dickinson et al.[60] We then employ an approach similar to that described by Newman and Thomas-Alyea,[50] where the intermediate species formed in Eq. 6 does not accumulate, and thus the current associated with the reaction in Eq. 6 must equal the current associated with the reaction in Eq. 7. If the heterogeneous rate constant associated with Eq. 7 is much greater than the rate constant associated with Eq. 6, the resulting current-overpotential relation may be written as

$$i = 2Fk^0\left\{c_{Mg}\exp\left[\frac{(2-\beta)F}{RT}\eta\right] - c_{Mg^{2+}}\exp\left[-\frac{\beta F}{RT}\eta\right]\right\} \quad [14]$$

where i is the current density, k^0 is the standard heterogeneous rate constant for the multistep reaction, β is the symmetry factor, and $\eta = E - \phi_0 - E^{0'}$ is the overpotential. Here, E is the potential of the WE (as compared to the RE), ϕ_0 is the electrostatic potential in the electrolyte immediately adjacent to the electrode, and $E^{0'}$ is the formal potential of the redox reaction at the equilibrium electrolyte concentration.

The kinetic rate law presented above is insufficient for capturing all of the essential features of the electrodeposition and electrodissolution of magnesium within the 1D model. Experimentally obtained CV curves for the electrodeposition and electrodissolution of magnesium to and from non-magnesium electrodes exhibit a hysteresis in the current density.[2,15,16,28,65] Towards the more reducing potentials of

the voltammogram, the onset of measurable current occurs later than would be expected, which is attributed to the effect of a nucleation overpotential associated with a free energy barrier for deposition.[4,65] In the oxidative region of the voltammogram, the current density increases until it abruptly drops to zero once all of the available magnesium has been dissolved from the WE. Experimentally, this drop-off occurs sooner than would be expected from the amount of magnesium deposited[28] because of Coulombic inefficiency. The following sections describe how both the nucleation overpotential and the Coulombic efficiency of the reaction process may be incorporated to supplement the kinetic rate law.

Nucleation.—As mentioned, there is an overpotential associated with the nucleation of magnesium deposits upon the WE surface, and this overpotential may be observed experimentally. In the kinetic rate law, the nucleation overpotential may be included as an additional term in the exponential. Experimental observations suggest that once a deposit has nucleated, no extra overpotential is necessary for its continued growth.[38] At any point during electrodeposition, nucleated deposits comprise a portion of the WE's surface area, with the balance being bare. The further nucleation and growth of deposits may both contribute to the measured current response, and as such, the kinetic rate law can be extended to represent a combination of the processes of deposit nucleation and subsequent growth:

$$i = 2Fk^0\left\{c_{\mathrm{Mg}}\theta\exp\left[\frac{(2-\beta)F}{RT}\eta\right] - c_{\mathrm{Mg^{2+}}}\left(\theta\exp\left[-\frac{\beta F}{RT}\eta\right] + (1-\theta)\exp\left[-\frac{\beta F}{RT}(\eta-\eta_{\mathrm{nuc}})\right]\right)\right\} \quad [15]$$

where θ is the fractional coverage of the bare WE surface by deposits and η_{nuc} is the nucleation overpotential.

Magnesium deposited from organohaloaluminate electrolytes has been observed to nucleate in a hexagonal plate morphology.[4,25] Unfortunately, the available micrographs for $Mg(BH_4)_2$ in tetraglyme only show the deposit morphology well after the initial nucleation process has completed.[24] Thus we assume that magnesium deposits from $Mg(BH_4)_2$/DME also nucleate as hexagonal plates with a constant ratio between the height and the deposit spacing; as these plates grow, they increasingly cover the WE surface and eventually merge. In this case, the value of θ is directly proportional to the average surface concentration of deposited magnesium, Γ_{dep}, until the deposits fully cover the WE and the fractional coverage reaches unity:

$$\theta = \begin{cases} \left(\frac{\Gamma_{\mathrm{dep}}(t)}{\Gamma_{\mathrm{ref}}}\right)^{\frac{2}{3}} & \Gamma_{\mathrm{dep}}(t) \le \Gamma_{\mathrm{ref}} \\ 1 & \Gamma_{\mathrm{dep}}(t) > \Gamma_{\mathrm{ref}} \end{cases} \quad [16]$$

Here, $\Gamma_{\mathrm{ref}} = rd/\Omega$ represents the surface concentration of magnesium at which the surface is fully covered, where r is the ratio between the deposit's height and the reference deposit edge length, d, and Ω is the molar volume of magnesium. The surface concentration of deposited magnesium relates to the current density through

$$\Gamma_{\mathrm{dep}}(t) = -\int_0^t \frac{i(t)}{2F}dt \quad [17]$$

Alternative assumptions can be made for the relationship between θ and Γ_{dep} to account for different deposit morphologies, which could be described in terms of their size, shape, and average spacing on the electrode surface. In future studies, it may also be desirable to account for the increased surface area of the electrode that would occur from the nucleation and growth of deposits; at present, it is assumed that this effect can be neglected.

Coulombic efficiency.—The 1D model also includes a phenomenological parameter that allows incorporation of the experimentally determined Coulombic efficiency, CE. This is defined as[15,16,66]

$$\mathrm{CE} = \frac{q_{\mathrm{diss}}^{\mathrm{tot}}}{q_{\mathrm{dep}}^{\mathrm{tot}}} \quad [18]$$

where $q_{\mathrm{diss}}^{\mathrm{tot}}$ is the total charge that passes across the WE during electrodissolution and $q_{\mathrm{dep}}^{\mathrm{tot}}$ is the total charge that passes across the WE during electrodeposition. Since the charge is related to the integral of the current, Eq. 18 can be rewritten as follows:

$$\mathrm{CE} = \frac{\int_0^t i_{\mathrm{diss}}(t)\,dt}{\int_0^t i_{\mathrm{dep}}(t)\,dt} = \frac{\int_0^t J_{\mathrm{diss}}^{\mathrm{Mg^{2+}}}(t)\,dt}{\int_0^t J_{\mathrm{dep}}^{\mathrm{Mg^{2+}}}(t)\,dt} \quad [19]$$

where $i_{\mathrm{diss}}(t)$ is the electrodissolution current, $i_{\mathrm{dep}}(t)$ is the electrodeposition current, and $J_{\mathrm{diss}}^{\mathrm{Mg^{2+}}}(t)$ and $J_{\mathrm{dep}}^{\mathrm{Mg^{2+}}}(t)$ are the fluxes of Mg^{2+} from and to the WE, respectively. These fluxes are obtained by splitting Eq. 15 into its electrodeposition and electrodissolution components and applying Faraday's Law:

$$J_{\mathrm{diss}}^{\mathrm{Mg^{2+}}}(t) = k^0 C_{\mathrm{Mg}}\theta\exp\left[\frac{(2-\beta)F}{RT}\eta\right] \quad [20]$$

$$J_{\mathrm{dep}}^{\mathrm{Mg^{2+}}}(t) = k^0 C_{\mathrm{Mg^{2+}}}\left\{\theta\exp\left[-\frac{\beta F}{RT}\eta\right] + (1-\theta)\exp\left[-\frac{\beta F}{RT}(\eta-\eta_{\mathrm{nuc}})\right]\right\} \quad [21]$$

A CE less than 1 (cf. Eq. 18) may arise from one or more processes in the cell that occur concurrently with the electrodeposition and electrodissolution of magnesium. In the experimental CV curves and electrochemical quartz crystal microbalance (EQCM) data presented by Lu et al.,[28] it seems reasonable to propose that these processes may be broadly categorized as one of two types. The first is a non-electrochemically active process that causes magnesium to be dissolved more quickly than expected (for example, magnesium becoming electronically isolated from the surface). The second is an electrochemically active process (such as a side reaction) during deposition that would contribute to the measured current, which would appear as if more magnesium was being deposited than in actuality. For our model, we assume a dominant process of the former type. Under the assumption that all deposited magnesium is subsequently dissolved from the WE, the following equation must hold:

$$\int_0^t J_{\mathrm{dep}}^{\mathrm{Mg^{2+}}}(t)\,dt = \int_0^t \left(J_{\mathrm{diss}}^{\mathrm{Mg^{2+}}}(t) + J_{\mathrm{side}}^{\mathrm{Mg^{2+}}}(t)\right)dt \quad [22]$$

Further, we assume that the flux of Mg^{2+} due to processes not included in the redox couple, $J_{\mathrm{side}}^{\mathrm{Mg^{2+}}}$, is directly proportional to the electrodissolution flux, $J_{\mathrm{diss}}^{\mathrm{Mg^{2+}}}$, with a proportionality constant ω. This allows Eq. 22 to be rewritten as:

$$\int_0^t J_{\mathrm{dep}}^{\mathrm{Mg^{2+}}}(t)\,dt = \int_0^t \left(J_{\mathrm{diss}}^{\mathrm{Mg^{2+}}}(t) + \omega J_{\mathrm{diss}}^{\mathrm{Mg^{2+}}}(t)\right)dt = M + \omega M \quad [23]$$

Equations 18 and 23 can be combined to determine the value of ω:

$$\omega = \frac{1}{\mathrm{CE}} - 1 \quad [24]$$

Finally, $i(t)$ in Eq. 17 is split into its components, $i_{\mathrm{diss}}(t)$ and $i_{\mathrm{dep}}(t)$, and $i_{\mathrm{diss}}(t)$ is multiplied by $(1+\omega)$:

$$\Gamma_{\mathrm{dep}}(t) = -\int_0^t \frac{(1+\omega)\,i_{\mathrm{diss}}(t) - i_{\mathrm{dep}}(t)}{nF}dt \quad [25]$$

which results in an expression of Γ_{dep} that is corrected for the effects of the Coulombic efficiency. Alternatively, if an additional electrochemically active process during deposition is dominant, one could

still arrive at ω as described by Eq. 24, but Γ_{dep} would revert to Eq. 17, and the total measured current would be greater by a factor of $1 + \omega$ than the actual deposition current.

Numerical methods.—Equations 1 through 3 are coupled nonlinear partial differential equations that are numerically stiff,[58–60,67] requiring small time step size if an explicit time stepping scheme were employed. Therefore, the equations are discretized using a semi-implicit Crank-Nicolson scheme that is second order in space and first order in time. The spatial grid is composed of 100 points whose positions are given by:

$$x_j = x_{j-1}\left(\frac{L}{\Delta x_0}\right)^{\frac{1}{N-2}} \quad [26]$$

where x_j is the j-th grid point position, $\Delta x_0 = 1$ Å is the minimum grid spacing, and N is the number of grid points. The grid point x_1 is at $-\Delta x_0$ and the grid point x_2 is at Δx_0. This generates a grid that has high resolution near the WE and lower resolution toward the RE, which ensures good numerical accuracy without sacrificing computational efficiency. At each grid point, five unknown quantities are defined: the concentrations of the four species (Mg^{2+}, $Mg(BH_4)^+$, BH_4^-, and undissociated $Mg(BH_4)_2$) in the electrolyte and the local electrostatic potential, ϕ. All of the unknown quantities are solved simultaneously using the Newton-Raphson method, as described by Brumleve and Buck[58] and Streeter and Compton.[59] The linear system for the Newton-Raphson iteration is solved using Gaussian Elimination with partial pivoting. A dimensionless scheme similar to those in the literature[58,60,68] was implemented to both improve the numerical accuracy and simplify the governing equations, the details of which may be found in the Supporting Information.

Fitting procedure.—The model described in the previous section is applied to construct a series of simulated CV curves. A semiautomatic procedure is adopted to determine the best-fitting parameters for the model. For each unknown parameter in the system, a batch-processing routine tests all possible combinations of parameters that are uniformly sampled from a discrete set within a range of values. For each simulated CV curve, the sum of squares of the difference with respect to the experimental data within a relevant portion of the voltage scan is calculated as a measure of the absolute error, which is minimized. For this study, the model simulates the CV curve between ±1 V applied potentials, and for the calculation of the error we consider the voltage range starting at 0 V (where the experimental sweep started), to the lower bound of −1 V, and then back to 0.2 V (just before the peak during electrodissolution). This voltage range was chosen for the error calculation because the model is unable to capture the observed dissolution behavior past 0.2 V, which is likely due to changes in the deposit morphology that are not considered by the present approximations. To reduce the number of degrees of freedom within the parameter space, all of the species arising from the dissociation of $Mg(BH_4)_2$ are taken to have equal diffusivity, D (consistent with the data reported by Rajput et al.[21]). In addition to D, the fitting procedure is used to obtain the values of the standard heterogeneous rate constant, k^0, the symmetry factor, β, the formal reaction potential, $E^{0'}$, and the nucleation overpotential, η_{nuc}, which appear in Eqs. 8 and 17.

This fitting procedure is applied to the first cycle of the experimentally obtained CV curve with a 20 mV/s voltage scan rate. An exploratory parameter sweep is performed to find the initial search range for subsequent parameter sweeps. A coarse parameter sweep is performed, and a histogram is generated of the parameter combinations whose sum of squared error (SSE) is less than 7×10^{-7} A^2/cm^4. This threshold value is chosen because it both encompasses the range of space where the likely parameters exist and results in voltammograms that are in good visual agreement with the experimental data. If a smaller tolerance is chosen, the histograms exhibit gaps in the peaks, which is due to an insufficient number of parameter sets that satisfy the tolerance at the coarse sampling resolution. The coarse histogram is then used to determine the bounds of a finer parameter sweep. To validate the model, we employ the resulting best-fit parameters to predict the behavior at the faster scan rates, which is then compared to the experimental data at the corresponding rates.

Experimental

Cyclic voltammetry experiments were performed under an Ar atmosphere in an Omnilab glove box (Vacuum Atmospheres, USA) with O_2 levels below 1 ppm and H_2O levels below 0.5 ppm. Dimethoxyethane (DME, 99.5%, Sigma Aldrich, USA) was stored over molecular sieves (3 Å, Fisher Scientific, USA) in the glove box for at least two days before the experiment to ensure dehydration. Magnesium borohydride ($Mg(BH_4)_2$, 95%, Sigma-Aldrich, USA) was stored in the glove box and used without further treatment. $Mg(BH_4)_2$ was dissolved in DME by stirring with a PTFE-coated magnetic stirbar for one hour at room temperature. An electrolyte with 75 mM concentration was prepared.

CV measurements were carried out in the glove box at room temperature using an Autolab PGSTAT302N potentiostat (Metrohm, Netherlands). A standard unstirred three-electrode electrochemical cell was employed, in which the reference compartment was connected to the working compartment by a Luggin capillary and the counter compartment was separated from the working compartment by a glass frit. The spacing between the counter electrode and WE was 7 cm, and the spacing between the RE and WE was 5 cm. The WEs were 100 μm diameter gold (99.998%, Alfa Aesar, USA) disk microelectrodes, produced in the laboratory by flame-sealing metal wires in soda-lime-glass capillary tubes. Counter electrodes and REs were comprised of magnesium foil (99%, Goodfellow, USA) and magnesium wire (99%, Goodfellow, USA), respectively. As discussed, this geometry is different from what is employed in the model, but for the purpose of demonstrating the capability of the model, it should be sufficient. Exterior surfaces of the magnesium electrodes were removed mechanically in the glove box prior to each experiment by scraping their surfaces with stainless steel scissors to expose shiny sub-surfaces. The WE potential was swept between ±1 V for ten cycles at voltage scan rates of 20, 50, and 100 mV/s starting at 0 V. Measured Coulombic efficiencies were low, with values of 34% at 20 mV/s, 39% at 50 mV/s, and 46% at 100 mV/s. Although multiple cycles were performed, only the first cycles of each scan rate were employed in the model parameterization. We note that the observed nucleation overpotential declined with each subsequent cycle in the experiments.

Results and Discussion

Parameter fitting and CV curve prediction.—The parameter spaces sampled and the numbers of sampling steps for the coarse and fine sweeps are summarized in Table I, and additional parameters required for the simulation are summarized in Table II. The sampling step size is equal for a given parameter and a given sweep. The coarse parameter sweep resulted in 38,880 combinations. The histogram for this sweep is shown as Fig. S1 in the supplemental information. At the coarse level, the parameters exhibit unresolved peaks due to the low sampling resolution. Therefore, a fine parameter sweep was performed with 136,890 possible combinations, of which 145 (or 0.11% of tested combinations) met the SSE threshold of 7×10^{-7} A^2/cm^4. The histograms of the distributions of parameters for these calculations are shown in Fig. 2. Compared to the coarse parameter sweep, the histograms in Fig. 2 exhibit well-defined peaks due to their finer resolution. The voltammograms are shown in Fig. 3 for the parameter sets that had the lowest overall SSE value as well as the highest value that was below the threshold. The SSE values and the parameter sets for these calculations are shown in Table III. The experimental CV curve and the simulated CV curve with the best-fit parameter set are in good agreement except toward the end of dissolution, where the

Table I. Parameter Spaces Examined by the Coarse and Fine Sweeps.

	coarse			fine		
parameter	low	high	# steps	low	high	# steps
β	0.15	0.55	9	0.225	0.425	9
k^0 (cm/s)	1.78×10^{-8}	1×10^{-6}	8†	1.78×10^{-8}	5.62×10^{-7}	13†
D (cm^2/s)	0.9×10^{-5}	1.7×10^{-5}	9	1.0×10^{-5}	1.6×10^{-5}	13
$E^{0'}$ (V)	−0.02	0.08	6	−0.01	0.07	9
η_{nuc} (V)	−0.65	−0.2	10	−0.65	−0.2	10

†Indicates logarithmic step sizes were used.

Table II. Additional Simulation Parameters.

parameter	Value
ϵ_s	7.2†
T	298 K
L	5 cm
Δt	0.1 s
K_{d1}	4.77×10^{-5} mol/cm^3
K_{d2}	4.77×10^{-3} mol/cm^3
c_{Mg}	7.14×10^{-2} mol/cm^3
Ω	14 cm^3/mol
r	0.125
d	160 nm

†Value taken from Ref. 73.

experimental data shows non-ideality, likely due to more complex deposit morphologies that are not accounted for in the model.

Using the best-fit parameter set, we predicted the voltammograms at the 50 and 100 mV/s voltage scan rates (shown in Figs. 4a and 4b). The predicted curves are again in good agreement with the experimental data for most of the voltage scan. In these cases, however, the slope of the simulated CV curves during electrodissolution better matched the experimental curves. In general, the predicted curves also show agreement with both the onset and cessation of deposition, although the peak deposition current is higher for the predicted curves than the experimentally observed peak current.

To estimate the uncertainties of the fitted parameters, the mean and standard deviation was calculated for each parameter, the values of which are summarized in Table IV. It is observed that the best-fit parameter set is within one standard deviation of the mean values. Comparison of the fitted parameters with experimental data is difficult because, as was mentioned previously, many of these parameters do not have reported values in the literature. However, we may make comparisons for both D and η_{nuc}. For D, the fitted value of 1.3×10^{-5} cm^2/s is about six times larger than the value of approximately 2×10^{-6} cm^2/s reported by Rajput et al.[21] While a value of η_{nuc} is not available for nucleating magnesium upon a gold substrate, literature values upon copper, platinum, nickel, and silver range from −240 mV to −850 mV,[4,37,38] and our fitted value of −300 mV is within the range. It should be noted that the predicted values of k^0 and η_{nuc} would depend on the assumed deposit geometry, as well as the cell geometry.

For the symmetry factor, β, the fitted value of 0.31 is lower than the value of 0.5 that has been measured previously for lithium deposition.[69] It is well-known that the charge transfer coefficient, and

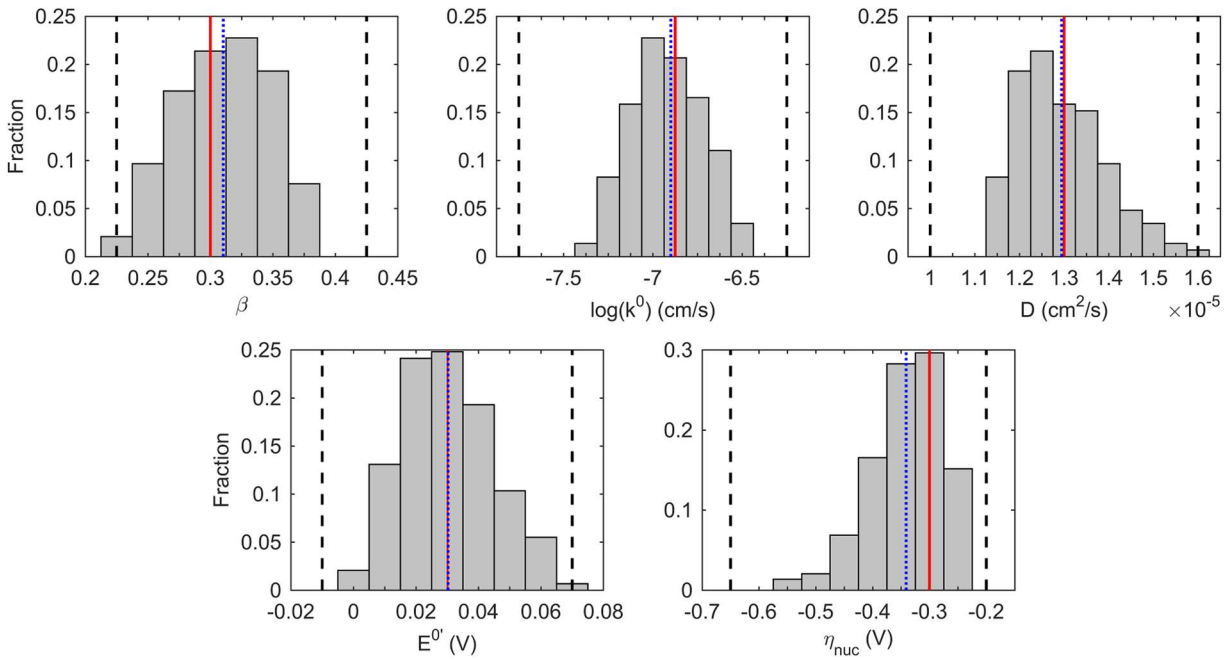

Figure 2. A histogram showing the distribution of parameters that result in simulated voltammograms with an SSE value below 7×10^{-7} A^2/cm^4 for 75 mM $Mg(BH_4)_2$ at 20 mV/s after the fine parameter sweep. The black dashed lines indicate the bounds of the parameter space. The solid red line indicates the best-fit value of the parameter, and the dash-dot blue line indicates the mean value of the parameter.

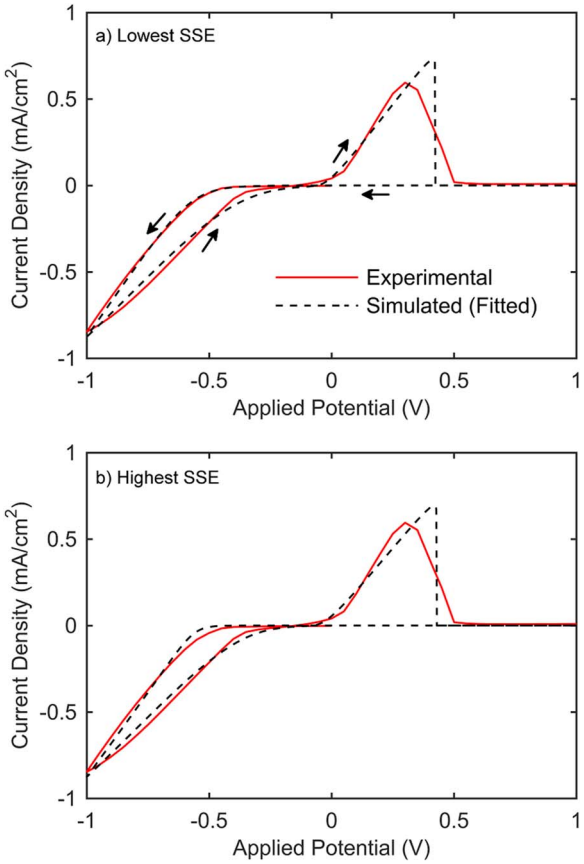

Figure 3. A comparison of the experimental (solid red) and simulated (dashed black) cyclic voltammograms for the 75 mM concentration at 20 mV/s for the combinations of the parameters that resulted in (a) the lowest sum of squared error and (b) the highest sum of squared error below the threshold of 7×10^{-7} A^2/cm^4. The parameters for each curve are reported in Table III.

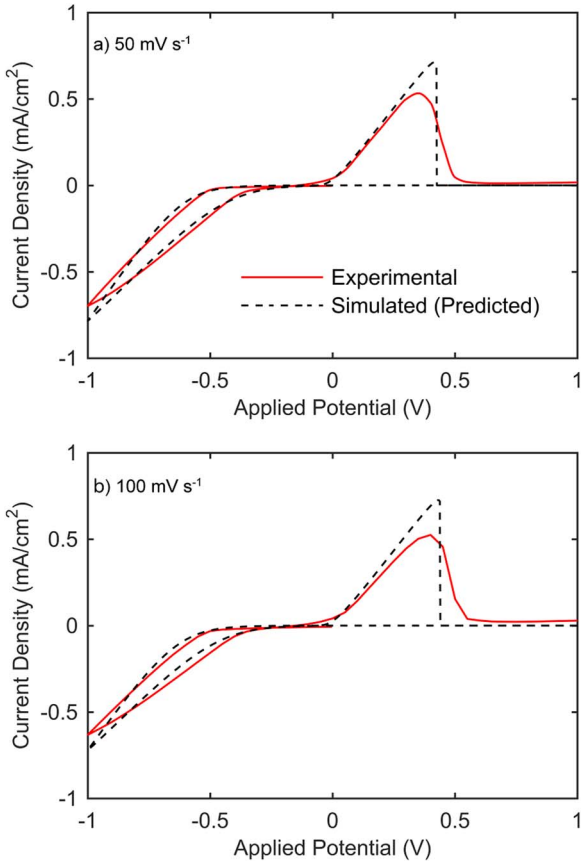

Figure 4. A comparison of the experimental (solid red) and simulated (dashed black) cyclic voltammograms for the 75 mM concentration at (a) 50 mV/s, and (b) 100 mV/s. The best-fit values that were obtained by fitting the 20 mV/s curve were then used to predict the behavior at higher sweep rates.

consequently the symmetry factor, depends upon the overall reaction mechanism.[70,71] Although the model is capable of isolating a likely value of β, the fitted value depends on the assumed reaction mechanism. Therefore, if the actual mechanisms differ from the assumed mechanism, the fitted value of β may not be representative. However, this does lead to the possibility of future investigations that could be performed with the described model to determine whether or not the calculated value of β is a consistent trend in magnesium electrochemistry.

Overall, the results demonstrate that while it is feasible to determine the parameters using the described fitting procedure, there is a moderate degree of uncertainty in the calculated parameters. However, the uncertainties would be reduced if one or more of the parameters—particularly the deposit morphology throughout the cycle—could be accurately determined experimentally. It should also be noted that there is an inherent error in the values summarized in Table IV because of the fact that the simulated cell geometry does not exactly correspond to the one used in the experiments reported in this work. However, the data is sufficient for the demonstration of the approach.

Effect of sweep rate on peak current.—Generally, an increase in the sweep rate is expected to lead to an increase in the magnitude of the peak currents in the voltammogram from non-faradaic processes.[52,60] However, both the experimental and simulated results in Figs. 3 and 4 exhibit a decrease in the magnitude of the peak current with increasing scan rate. We propose that the decrease in peak current is due to a smaller amount of electrochemically active magnesium and not non-faradaic behavior of the electrolyte. In Fig. 5, it is observed that as the sweep rate increases, there is a corresponding decrease in the simulated value of θ at the peak deposition current. This is primarily a result of the shorter duration of the cycle at higher voltage scan rates within the same fixed voltage range. As stated in Eq. 25, the total amount of deposited magnesium is related to the time integral of the current. Thus, at higher rates, less magnesium is deposited even if the current at a given voltage is otherwise the same.

Table III. Parameters Describing the Lowest and Highest SSE Fits.

	parameter values	
Parameter	lowest SSE	highest SSE
SSE (A^2/cm^4)	5.32×10^{-7}	6.99×10^{-7}
β	0.3	0.375
k^0 (cm /s)	1.33×10^{-7}	5.62×10^{-8}
D (cm^2/s)	1.3×10^{-5}	1.2×10^{-5}
$E^{0'}$ (V)	0.03	0.01
η_{nuc} (V)	−0.3	−0.5

Table IV. Average Parameter Values Fitted by Model.

parameter	average value
β	0.31 ± 0.04
k^0 (cm/s)	$1.3 \pm 0.4 \times 10^{-7}$
D (cm^2/s)	$1.3 \pm 0.1 \times 10^{-5}$
$E^{0'}$ (V)	0.030 ± 0.015
η_{nuc} (V)	-0.34 ± 0.07

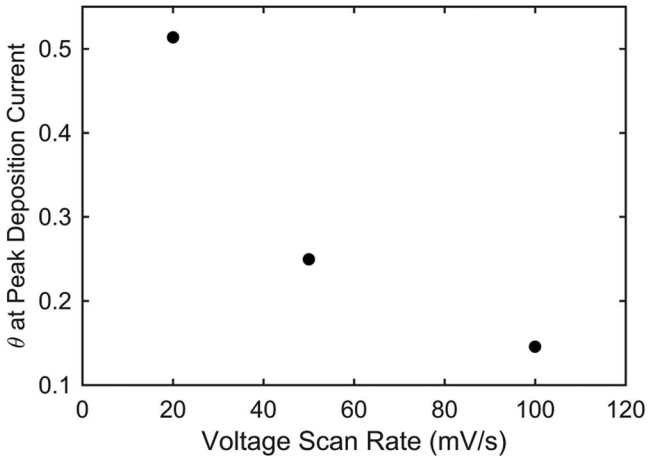

Figure 5. A plot of the fraction of the surface area covered by magnesium, θ, at the peak deposition current as a function of the sweep rate. At higher sweep rates, less material can be deposited due to the shorter duration of the cycle, reducing the coverage by magnesium.

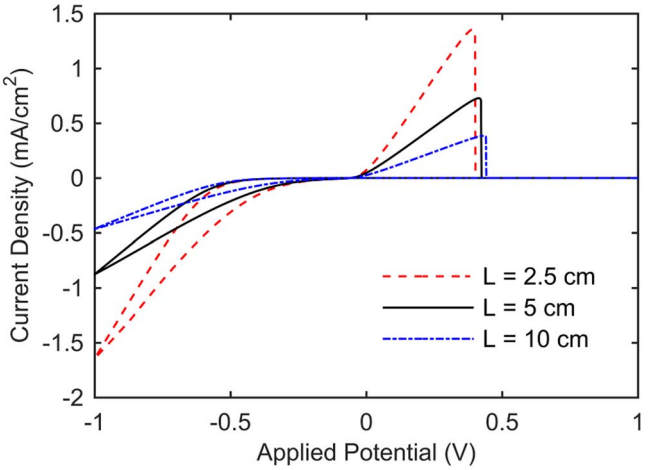

Figure 6. The impact of the spacing between the WE and RE in the model. As the spacing increases, the measured current response to the voltage sweep decreases. These curves were calculated using the parameters for the 75 mM electrolyte at 20 mV/s.

While the model agrees with the experimentally observed trend of a decreasing peak current with increasing sweep rate, the model predicts a smaller magnitude of decrease than is experimentally observed. The likely cause of this discrepancy is that the actual deposit morphology is more complex than that assumed in the model. By inspection of Eq. 15, the deposition behavior may be split into two limiting cases: deposition purely by growth of existing deposits or by nucleation of new deposits. The nucleation overpotential lowers the formal potential of the reaction, which shifts the voltammetric behavior to more negative applied potentials. Thus, at a given negative applied potential, deposition by nucleation would yield a lower current than deposition by growth. It can be observed from the simulation that θ serves to shift the deposition curve in between these two extremes. Therefore, we conclude that the assumed nucleation model overestimates the active amount of magnesium, and consequently the current is predicted to be higher than is observed experimentally. Future experimental work may be able to inform the model regarding more realistic morphology of the magnesium deposits, which may depend on the voltage scan rate.

Considerations of experimental geometry.—Using the parameters predicted by the model, we also predict the response of the voltammogram to changes in the spacing between the WE and the RE. For this test, we calculated the voltammogram for a 75 mM electrolyte at a voltage scan rate of 20 mV/s, assuming spacings of 2.5 cm, 5 cm (the actual experimental spacing), and 10 cm using the parameters given in Table III. The resulting curves are plotted in Fig. 6, where the magnitude of the measured current decreases as the electrode spacing increases. This relationship is of the form $i \propto 1/L$, where L is the WE/RE spacing; halving the electrode spacing roughly doubles the measured current density at a given point, and doubling the spacing halves the measured current density. Therefore, the model indicates that when using electrodes that are large as compared to the separation between them, the spacing between the WE and RE must be known in order to accurately determine the dynamics of the system. This behavior arises from the uncompensated resistance of the poorly conductive unsupported electrolyte. This is in agreement with the report by Myland and Oldham,[72] which concluded that, for a weakly conductive electrolyte, the uncompensated resistance will always have an effect on the measured cell behavior unless the separation between the WE and RE becomes infinitesimally small. Thus, the cell geometry should always be reported for experimental measurements of voltammetry with unsupported electrolytes.

Conclusions

A 1D model was developed to simulate the cyclic voltammetry of a $Mg(BH_4)_2$/DME electrolyte with a gold WE and a magnesium RE by simultaneously solving the Nernst-Planck and Poisson equations for the mass transport and electrostatic potential, respectively. Boundary conditions were developed to incorporate a kinetic rate law for magnesium deposition and dissolution, which was modified to account for the nucleation behavior of magnesium upon the WE and the experimentally determined Coulombic efficiency. This model was parameterized by batch fitting to the first cycle of experimentally obtained voltammograms for 75 mM concentration of electrolyte at 20 mV/s. The fitted parameters were employed to predict the voltammetric response at 50 and 100 mV/s. Histograms of the parameter sets that produce good fits to the experimental voltammograms over a large parameter space were generated. The results show that the model is able to predict a likely range of the parameters that describe the system. The best-fit values of the parameters produce cyclic voltammograms that are overall similar to the experimental curves against which they were fit, and the predicted voltammograms at higher sweep rates also exhibit good agreement with the experimental data.

The model, combined with the fitting procedure, allowed for the determination of kinetic information of the $Mg(BH_4)_2$/DME electrolyte, but this was made possible by employing several assumptions to minimize degrees of freedom in the system of equations. First, it was assumed that the electrolyte was mostly dissociated into solvated ions and the electroactive species was Mg^{2+}. Second, convection was assumed not to contribute to mass transport. Third, the development of the kinetic rate law assumed that the rate constant for the formation of the intermediate was significantly faster than for the deposition of the solid and thus could be neglected in the overall expression. Fourth, a simple deposit morphology was assumed to describe the surface of the WE due to a lack of available experimental data. Fourth, the Coulombic efficiency below unity was assumed to arise from a non-electrochemical process that occurs during dissolution. Fifth, all solute diffusivities were assumed to be equal. Finally, experimental data with a planar cell geometry were not available, and thus a data set obtained with a disk microelectrode and comparatively larger counter and reference electrodes was utilized. Based on the present simulation results, an experimental setup with a planar electrode geometry where the electrodes are large with respect to the separation between them appears to be a viable scheme for extracting the parameters governing reaction kinetics and mass transport. In addition, the electrode separation must be accurately measured and reported for such a setup because it plays a key role in the dynamic behavior captured by the

voltammogram. There are also moderate uncertainties in the average values of some of the fitted parameters, which are likely due to interplay between the surface deposit morphology, nucleation overpotential, and standard heterogeneous rate constant. With experimental work to accurately measure values of even one or two parameters, the uncertainties in the remaining parameters should decrease greatly.

Acknowledgment

This work was supported as part of the Joint Center for Energy Storage Research, an Energy Innovation Hub funded by the U.S. Department of Energy, Office of Science, Basic Energy Sciences. Additionally, this research used resources of the National Energy Research Scientific Computing Center, a DOE Office of Science User Facility supported by the Office of Sciences of the U.S. Department of Energy under Contract No. DE-AC02-05CH11231.

References

1. T. D. Gregory, R. J. Hoffman, and R. C. Winterton, *J. Electrochem. Soc.*, **137**, 775 (1990).
2. D. Aurbach, Z. Lu, A. Schechter, Y. Gofer, H. Gizbar, R. Turgeman, Y. Cohen, M. Moshkovich, and E. Levi, *Nature*, **407**, 724 (2000).
3. H. D. Yoo, I. Shterenberg, Y. Gofer, G. Gershinsky, N. Pour, and D. Aurbach, *Energy Environ. Sci.*, **6**, 2265 (2013).
4. M. Matsui, *J. Power Sources*, **196**, 7048 (2011).
5. D. Aurbach, Y. Gofer, Z. Lu, A. Schechter, O. Chusid, H. Gizbar, Y. Cohen, V. Ashkenazi, M. Moshkovich, and R. Turgeman, *J. Power Sources*, **97–98**, 28 (2001).
6. C. Liebenow, Z. Yang, and P. Lobitz, *Electrochem. commun.*, **2**, 641 (2000).
7. D. Aurbach, H. Gizbar, A. Schechter, O. Chusid, H. E. Gottlieb, Y. Gofer, and I. Goldberg, *J. Electrochem. Soc.*, **149**, A115 (2002).
8. A. Benmayza, M. Ramanathan, T. S. Arthur, M. Matsui, F. Mizuno, J. Guo, P.-A. Glans, and J. Prakash, *J. Phys. Chem. C*, **117**, 26881 (2013).
9. F. Mizuno, N. Singh, T. S. Arthur, P. T. Fanson, M. Ramanathan, A. Benmayza, J. Prakash, Y.-S. Liu, P.-A. Glans, and J. Guo, *Front. Energy Res.*, **2**, 1 (2014).
10. T. J. Carter, R. Mohtadi, T. S. Arthur, F. Mizuno, R. Zhang, S. Shirai, and J. W. Kampf, *Angew. Chemie*, **126**, 3237 (2014).
11. C. J. Barile, R. Spatney, K. R. Zavadil, and A. A. Gewirth, *J. Phys. Chem. C*, **118**, 10694 (2014).
12. C. J. Barile, E. C. Barile, K. R. Zavadil, R. G. Nuzzo, and A. A. Gewirth, *J. Phys. Chem. C*, **118**, 27623 (2014).
13. J. Muldoon, C. B. Bucur, A. G. Oliver, T. Sugimoto, M. Matsui, H. S. Kim, G. D. Allred, J. Zajicek, and Y. Kotani, *Energy Environ. Sci.*, **5**, 5941 (2012).
14. J. Muldoon, C. B. Bucur, A. G. Oliver, J. Zajicek, G. D. Allred, and W. C. Boggess, *Energy Environ. Sci.*, **6**, 482 (2013).
15. R. Mohtadi, M. Matsui, T. S. Arthur, and S.-J. Hwang, *Angew. Chemie Int. Ed.*, **51**, 9780 (2012).
16. Y. Shao, T. Liu, G. Li, M. Gu, Z. Nie, M. Engelhard, J. Xiao, D. Lv, C. Wang, J.-G. Zhang, and J. Liu, *Sci. Rep.*, **3**, 3130 (2013).
17. Y. Shao, M. Gu, X. Li, Z. Nie, P. Zuo, G. Li, T. Liu, J. Xiao, Y. Cheng, C. Wang, J.-G. Zhang, and J. Liu, *Nano Lett.*, **14**, 255 (2014).
18. T. Liu, Y. Shao, G. Li, M. Gu, J. Hu, S. Xu, Z. Nie, X. Chen, C. Wang, and J. Liu, *J. Mater. Chem. A*, **2**, 3430 (2014).
19. S. H. Lapidus, N. N. Rajput, X. Qu, K. W. Chapman, K. A. Persson, and P. J. Chupas, *Phys. Chem. Chem. Phys.*, **16**, 21941 (2014).
20. I. Shterenberg, M. Salama, Y. Gofer, E. Levi, and D. Aurbach, *MRS Bull.*, **39**, 453 (2014).
21. N. N. Rajput, X. Qu, N. Sa, A. K. Burrell, and K. A. Persson, *J. Am. Chem. Soc.*, **137**, 3411 (2015).
22. T. Kakibe, J. Hishii, N. Yoshimoto, M. Egashira, and M. Morita, *J. Power Sources*, **203**, 195 (2012).
23. S.-Y. Ha, Y.-W. Lee, S. W. Woo, B. Koo, J.-S. Kim, J. Cho, K. T. Lee, and N.-S. Choi, *ACS Appl. Mater. Interfaces*, **6**, 4063 (2014).
24. F. Tuerxun, Y. Abulizi, Y. NuLi, S. Su, J. Yang, and J. Wang, *J. Power Sources*, **276**, 255 (2014).
25. S. DeWitt, N. Hahn, K. Zavadil, and K. Thornton, *J. Electrochem. Soc.*, **163**, A513 (2016).
26. G. Vardar, A. E. S. Sleightholme, J. Naruse, H. Hiramatsu, D. J. Siegel, and C. W. Monroe, *ACS Appl. Mater. Interfaces*, **6**, 18033 (2014).
27. R. E. Doe, R. Han, J. Hwang, A. J. Gmitter, I. Shterenberg, H. D. Yoo, N. Pour, and D. Aurbach, *Chem. Commun. (Camb).*, **50**, 243 (2014).
28. Z. Lu, A. Schechter, M. Moshkovich, and D. Aurbach, *J. Electroanal. Chem.*, **466**, 203 (1999).
29. N. Kumar and D. J. Siegel, *J. Phys. Chem. Lett.*, **7**, 874 (2016).
30. N. W. Kondyrew and D. P. Manojew, *Ber. Dtsch. Chem. Ges.*, **58**, 464 (1925).
31. W. V. Evans and F. H. Lee, *J. Am. Chem. Soc.*, **55**, 1474 (1933).
32. W. V. Evans, F. H. Lee, and C. H. Lee, *J. Am. Chem. Soc.*, **57**, 489 (1935).
33. R. E. Dessy and R. M. Jones, *J. Org. Chem.*, **24**, 1685 (1959).
34. L. Martinot, *Bull. des Soc. Chim. Belges*, **75**, 711 (1966).
35. L. Martinot, *Bull. des Soc. Chim. Belges*, **76**, 617 (1967).
36. D. J. Wetzel, M. A. Malone, R. T. Haasch, Y. Meng, H. Vieker, N. T. Hahn, A. Gölzhäuser, J.-M. Zuo, K. R. Zavadil, A. A. Gewirth, and R. G. Nuzzo, *ACS Appl. Mater. Interfaces*, **7**, 18406 (2015).
37. J. D. Genders and D. Pletcher, *J. Electroanal. Chem.*, **199**, 93 (1986).
38. Z. Feng, Y. NuLi, J. Wang, and J. Yang, *J. Electrochem. Soc.*, **153**, C689 (2006).
39. D. Wheeler, D. Josell, and T. P. Moffat, *J. Electrochem. Soc.*, **150**, C302 (2003).
40. J. E. Guyer, W. J. Boettinger, J. A. Warren, and G. B. McFadden, *Phys. Rev. E*, **69**, 21603 (2004).
41. J. E. Guyer, W. J. Boettinger, J. A. Warren, and G. B. McFadden, *Phys. Rev. E*, **69**, 21604 (2004).
42. Y. Shibuta, Y. Okajima, and T. Suzuki, *Sci. Technol. Adv. Mater.*, **8**, 511 (2007).
43. D. R. Ely and R. E. Garcia, *J. Electrochem. Soc.*, **160**, A662 (2013).
44. L. Liang and L.-Q. Chen, *Appl. Phys. Lett.*, **105**, 263903 (2014).
45. D. R. Ely, A. Jana, and R. E. García, *J. Power Sources*, **272**, 581 (2014).
46. D. A. Cogswell, *Phys. Rev. E*, **92**, 11301 (2015).
47. M. Planck, *Ann. der Phys. und Chemie*, **275**, 161 (1890).
48. M. Planck, *Ann. der Phys. und Chemie*, **276**, 561 (1890).
49. M. Planck, *Z. Phys.*, **94**, 469 (1935).
50. J. Newman and K. E. Thomas-Alyea, *Electrochemical Systems*, Third edition., Wiley Interscience, Hoboken, New Jersey, (2004).
51. F. G. Cottrell, *Z. Phys. Chem.*, **42**, 385 (1903).
52. A. J. Bard and L. R. Faulkner, *Electrochemical Methods: Fundamentals and Applications*, Second., John Wiley & Sons, Inc., Hoboken, New Jersey, (2001).
53. R. S. Nicholson and I. Shain, *Anal. Chem.*, **36**, 706 (1964).
54. E. J. F. Dickinson, J. G. Limon-Petersen, and R. G. Compton, *J. Solid State Electrochem.*, **15**, 1335 (2011).
55. H. Wang, A. Thiele, and L. Pilon, *J. Phys. Chem. C*, **117**, 18286 (2013).
56. H. Cohen and J. W. Cooley, *Biophys. J.*, **5**, 145 (1965).
57. J. R. Sandifer and R. P. Buck, *J. Phys. Chem.*, **79**, 384 (1974).
58. T. R. Brumleve and R. P. Buck, *J. Electroanal. Chem. Interfacial Electrochem.*, **90**, 1 (1978).
59. I. Streeter and R. G. Compton, *J. Phys. Chem. C*, **112**, 13716 (2008).
60. E. J. F. Dickinson, J. G. Limon-Petersen, N. V Rees, and R. G. Compton, *J. Phys. Chem. C*, **113**, 11157 (2009).
61. H. Noth, *Angew. Chemie*, **73**, 371 (1961).
62. A. E. Shirk and D. F. Shriver, *J. Am. Chem. Soc.*, **95**, 5901 (1973).
63. E. J. F. Dickinson and R. G. Compton, *Chem. Phys. Lett.*, **497**, 178 (2010).
64. R. He, S. Chen, F. Yang, and B. Wu, *J. Phys. Chem. B*, **110**, 3262 (2006).
65. C. Liebenow, *J. Appl. Electrochem.*, **27**, 221 (1997).
66. D. Aurbach, G. S. Suresh, E. Levi, A. Mitelman, O. Mizrahi, O. Chusid, and M. Brunelli, *Adv. Mater.*, **19**, 4260 (2007).
67. J. G. Limon-Petersen, I. Streeter, N. V. Rees, and R. G. Compton, *J. Phys. Chem. C*, **113**, 333 (2009).
68. M. Z. Bazant, K. Thornton, and A. Ajdari, *Phys. Rev. E*, **70**, 21506 (2004).
69. M. W. Verbrugge and B. J. Koch, *J. Electrochem. Soc.*, **141**, 3053 (1994).
70. J. O. Bockris and Z. Nagy, *J. Chem. Educ.*, **50**, 839 (1973).
71. R. Guidelli, R. G. Compton, J. M. Feliu, E. Gileadi, J. Lipkowski, W. Schmickler, and S. Trasatti, *Pure Appl. Chem.*, **86**, 245 (2014).
72. J. C. Myland and K. B. Oldham, *Anal. Chem.*, **72**, 3972 (2000).
73. J. A. Riddick and W. B. Bunger, *Organic Solvents: Physical Properties and Methods of Purification*, 3rd ed., Wiley Interscience, New York (1970).